Lamin B Distribution and Association with Peripheral Chromatin Revealed by Optical Sectioning and Electron Microscopy Tomography

Andrew S. Belmont, Yuan Zhai, and Anja Thilenius

Department of Cell and Structural Biology, University of Illinois, Champaign-Urbana, Urbana, Illinois 61801

Abstract. We have used a combination of immunogold staining, optical sectioning light microscopy, intermediate voltage electron microscopy, and EM tomography to examine the distribution of lamin B over the nuclear envelope of CHO cells. Apparent inconsistencies between previously published light and electron microscopy studies of nuclear lamin staining were resolved. At light microscopy resolution, an apparent open fibrillar network is visualized. Colocalization of lamin B and nuclear pores demonstrates that these apparent fibrils, separated by roughly 0.5 μm, are anti-correlated with the surface distribution of nuclear pores; pore clusters lie between or adjacent to regions of heavy lamin B staining. Examination at higher, EM resolution reveals that this apparent lamin B network does not correspond to an actual network of widely spaced, discrete bundles of lamin filaments. Rather it reflects a quantitative variation in lamin staining over a roughly 0.5-μm size scale, superimposed on a more continuous but still complex distribution of lamin filaments, spatially heterogeneous on a 0.1–0.2-μm size scale. Interestingly, lamin B staining at this higher resolution is highly correlated to the underlying chromatin distribution. Heavy concentrations of lamin B directly "cap" the surface of envelope associated, large-scale chromatin domains.

OVER the last 15 years the concept of a karyskeleton, or nuclear scaffolding, has emerged (Fisher, 1989). To date, however, the only nuclear proteins established as filamentous proteins are the nuclear lamins, a major component of the nuclear lamina. Initial identification of lamins as a new class of intermediate filament proteins came largely from sequence homology data (Fisher et al., 1986; McKeon et al., 1986) and structural studies on in vitro reconstituted lamin filaments (Aebi et al., 1986). Subsequent molecular and biochemical characterization of the nuclear lamins has proceeded rapidly, as reviewed recently (Newport et al., 1987; Gerace et al., 1988; Nigg, 1989; McKeon, 1991; Nigg, 1992).

Two types of nuclear lamin proteins have been classified functionally; the first, consisting of lamins A and C in mammalian somatic cells, are solubilized completely during mitosis, while the second class, consisting of lamin B in mammalian somatic cells, remains associated with membrane vesicles (Gerace et al., 1980; Burke et al., 1986). In *Drosophila melanogaster* only one nuclear lamin, belonging to the second class, has been identified to date (Gruenbaum et al., 1988).

Biochemical and genetic data suggest interaction between nuclear lamins and chromatin. For a mammalian, cell-free nuclear assembly system, coating of chromosomes by lamins precedes nuclear envelope formation, and depletion of lamins A and C or lamin B from the extract blocks both nuclear envelope formation and chromosome decondensation (Burke et al., 1986); in vivo experiments in which antibodies against lamins A, B, and C are injected into mammalian mitotic cells also show an inhibition of chromosome decondensation with lamin depletion (Benavente et al., 1987). In more purified systems, addition of mitotic chromosomes has been shown to lower the critical concentration for lamin A and C polymerization, and this polymerization occurs on the surface of the mitotic chromosomes (Burke, 1990; Glass et al., 1990). Lamin A also has been shown to bind to purified chromatin (Hoger et al., 1991; Yuan et al., 1991). More recently, lamin BI has been implicated as a binding protein for matrix attachment regions (MAR) DNA sequences (Luderus et al., 1992). In vivo, mutation of the lamin gene in *D. melanogaster* is embryonic recessive lethal; embryos homozygous for a lamin deletion show a phenotype with abnormal nuclear structure, including detachment of chromatin from the nuclear periphery (Dr. Yosef Gruenbaum, The Hebrew University of Jerusalem, personal communication).

In comparison to the molecular characterization accomplished to date, structural analysis of the nuclear lamins and lamina has lagged far behind. The most direct visualization of the nuclear lamina has been from hand-dissected *Xenopus* oocyte nuclear membranes (Aebi et al., 1986) and showed a tightly packed, square lattice of filaments in selected, and presumably better preserved, lamina regions. Spacing between filaments was about 50 nm. Lower resolution, anti-

Address all correspondence to Dr. A. Belmont, Department of Cell and Structural Biology, 506 Morrill Hall, 505 S. Goodwin Ave., University of Illinois, Champaign-Urbana, Urbana, IL 61801.

lamin immunostaining of thin sections from diploid, somatic nuclei (Gerace et al., 1978, 1981) suggested continuous staining, consistent with the oocyte observations. However, a recent three-dimensional optical sectioning light microscopy study (Paddy et al., 1990) instead suggested a highly discontinuous network with spacing of ~0.5 μm between network components. This lamin network was aligned, at low resolution, with DAPI-stained peripheral chromatin; however, most chromatin sites were offset in distance by ~0.15–0.25 μm, implying an indirect linkage of lamin and chromatin except for a small number of special chromosomal locations.

These apparent contradictions between previous light and electron microscopy studies, as well as in vitro biochemical results, underscore the technical difficulties in general associated with analysis of nuclear structure. To resolve these apparent inconsistencies, we have used a combination of immunogold staining, optical sectioning light microscopy, intermediate voltage EM, and EM tomography to examine the distribution of lamin B over the nuclear envelope of CHO cells. We focused on an intermediate resolution size scale, capable of extending the limited resolution of light microscopy while still allowing three-dimensional analysis of large nuclear volumes.

Materials and Methods

Immunostaining Procedure

CHO cells were plated at 16,000 cells/square cm on Aclar plastic coverslips (Pro-Plastics, Linden, NJ) for immunogold staining and on No. 1 1/2 glass coverslips for immunofluorescence staining. Two days later, with cells in log phase, the coverslips were rinsed 2× with cold buffer A, 80 mM KCl, 20 mM NaCl, 2 mM EDTA, 0.5 mM EGTA, 15 mM Pipes buffer, 15 mM β-mercaptoethanol, 0.5 mM spermidine, 0.2 mM spermine, 10 μg/ml turkey egg white protease inhibitor (Sigma Immunochemicals, St. Louis, MO), adjusted to pH 7.0. This was followed by a 20-s permeabilization using 0.1% digitonin and 0.16% Brij 58 in cold buffer A. For immunogold staining, 8% glutaraldehyde (Polysciences, Warrington, PA) was added then directly to the petri dishes to yield a final concentration of 0.1%; fixation was for 20 min at 4°C. For staining with fluorescent secondary antibodies, fixation instead used 1.6% formaldehyde (Polysciences) for 8 min at room temperature.

All remaining steps, prior to the second fixation step immediately preceding silver staining, were carried out at 4°C.

Three washes, 5 min each, were done in buffer A. Aldehyde groups were quenched using 20 mM glycine in buffer A during three washes, 5-min each. Buffer A* (buffer A without β-mercaptoethanol) with 5% normal goat serum was then applied for 1 h for blocking of nonspecific sites. An affinity-purified, rabbit polyclonal antibody directed against a carboxyl peptide of lamin B (Sobatka-Briner et al., 1992), a gift from Dr. Dan Chelsky (Dupont, Wilmington, DE), was used as the primary antibody at a 1/1,000 titer in buffer A* plus 0.1% Triton X-100 (Pierce). For double labeling against lamin B and nuclear pores, a mouse IgM mAb, RL1, from Dr. Larry Gerace (The Scripps Research Institute, La Jolla, CA) was used at a 1:200 dilution. This antibody is directed against a group of nuclear pore glycoproteins (Snow et al., 1987).

Following a 4–5-h incubation with primary, three washes in buffer A* with 0.1% Triton X-100 were done, each for 10 min. For immunogold staining, a secondary, 1 nm colloidal gold-labeled goat anti-rabbit antibody (Biocell) was then applied in buffer A* with 0.1% Triton X-100 at a 1/25–1/50 dilution. For immunofluorescence staining, secondary antibodies (Jackson Lab) at 1/500 dilution (GAM IgM FITC labeled) and 1/1,000 (GAR IgG Texas red labeled) were used in the same buffer. Overnight incubation in the secondary antibody was followed again by washes in buffer A* with 0.1% Triton X-100 as described above for the primary.

These washes were followed by a rinse in buffer A*. Immunogold-labeled specimens were then postfixed with 1% glutaraldehyde in buffer A for 1 h at room temperature. Samples were then washed 3 × 5 min in double-distilled H_2O, and silver stained (Dancher, 1981). Incubation in the Dancher developer varied from 10–15 min. Specimens stained for immunofluorescence were not postfixed. They were stepped through a glycerol/buffer A* series ending with 90% glycerol containing 3.5% *n*-propyl-gallate as an antifading agent (Giloh et al., 1983).

Small pieces of the immunogold-labeled Aclar coverslips were routinely mounted on glass slides and surveyed by light microscopy, allowing easy monitoring of staining intensity and background.

Sample Preparation for Electron Microscopy

Dehydration in EtOH and embedding in Epon or Epon/Araldite resins was carried out by standard methods, as described previously (Belmont et al., 1989). After infiltration in 100% resin, a drop of resin was sandwiched between the Aclar coverslip and a 2nd piece of Aclar. Resin polymerization was at 45°C overnight, followed by 48 h at 60°C. After resin polymerization, the two pieces of Aclar were peeled off, leaving an Epon wafer with the cell monolayer embedded on one surface.

Pieces of this Epon wafer were mounted on precast Epon blocks using Superglue. Thin and semi-thick sections were cut using a Standard or Semi diamond knife (Diatome U.S., Fort Washington, PA), using a Reichert Ultracut E ultramicrotome (Reichert Jung, Vienna). Sections were placed onto formvar-coated copper grids. For tomographic reconstructions, short ribbons were picked up on 50 × 200-mesh grids. Short ribbons increased section stability during beam exposure while 50 × 200-mesh grids allowed minimization of shadowing by grid bars at high-tilt angles while still providing adequate specimen support.

Grids were either unstained or stained from both sides with 0.2% uranyl acetate in 50% EtOH. Thin sections were poststained in 0.02% lead citrate. Semi-thick sections for tomography were not poststained with lead, so as to decrease the chromatin contrast. Before tomographic reconstructions, both section surfaces were coated with poly-L-lysine and 500-Å-diam gold beads, as described previously (Belmont et al., 1987), and then carbon coated.

Light Microscopy

For examination of silver-enhanced, immunogold-labeled samples, a Zeiss, laser scanning confocal microscope was used in the epi-illumination mode. Small pieces of the Epon wafer containing the immunogold-stained cell monolayer were mounted in H_2O on a glass slide using a No. 1 1/2 glass coverslip, cells facing up. A fluorescein filter set with the barrier filter removed was used with 488 nm laser illumination; the incomplete reflection of 488 nm light by the dichroic mirror gave rise to a strong scattered light from the silver-enhanced immunogold samples.

Complete optical section focus series were taken of three nuclei at 0.2-μm intervals using a 63×, 1.4 NA Planapochromat lens. Pixel size varied between 0.46 and .069 μm. Data sets were transferred to a DEC Microvax 3200 for image processing. Quadratic interpolation was used to resize all data sets to the same magnification.

For immunofluorescence observations, a conventional Olympus inverted light microscope (IMT-2) equipped with a Photometrics cooled, slow-scan CCD camera was used. This system duplicates one built by Drs. Agard and Sedat (University of California, San Francisco, CA) and has been described elsewhere (Hiraoka et al., 1991). Briefly, it includes motorized filter wheels for excitation and emission filters (Omega Optical Inc., Brattleboro, VT) and a microstepping motor for z focus, with a Silicon Graphics 4D/35TG computer providing automated data collection. A single quadruple dichroic mirror (Omega Optical Inc.) greatly minimizes x-y translational shifts between images collected at different wavelengths. A 60×, 1.4 NA Plan Apo oil immersion lens (Olympus) was used together with narrow pass filters for FITC and Texas Red excitation and emission. Optical sections were collected through entire nuclei at 0.2 μm focal intervals; pixel size was 0.074 μm and 512 × 512 pixel images were taken. Deconvolution of optical sections, to partially restore the image degradation resulting from out-of-focus blur, was accomplished using an enhanced ratio, iterative constrained deconvolution algorithm (Agard et al., 1989).

Using the deconvolved data, running averages of 15 optical sections (3.0 μm) were computed for each wavelength. Images representing the projection of the top or bottom of a nucleus were then selected for each wavelength data set. This approach simultaneously allowed visualization of a large projected nuclear surface area while minimizing problems related to focus offsets between multiple wavelength data and z axis blurring.

Registration in the x-y image plane of the double-stained images was checked using two methods. A Fourier-based cross-correlation approach,

which included determination of the differential magnification yielding the highest cross-correlation, indicated translational alignment of FITC and Texas red data was already within 1 pixel. The rationale for using cross-correlation methods to align two staining patterns, nuclear pore and lamin, which were likely to be different was based on the bright, near continuous staining pattern showed by both in the projected nuclear ring encircling the nuclei. Because of the shape of the nuclei and the z axis blurring, significant apparent overlapping of lamin and pore staining occurs at the nuclear periphery of the projected nuclear images which we expected would dominate the cross-correlation function. The second method used was visual inspection of the overlap of nuclear perimeters from the FITC and Texas red images of several nuclei positioned at opposite sides of the 512 × 512 pixel field; this method also suggested excellent registration between the FITC and Texas red images. These results are consistent with previous, more accurate measurements using multi-colored fluorescent beads with a similar microscope system, also using a single dicroic mirror (Agard et al., 1989); these measurements showed chromatic magnification changes of roughly 0.2% and image translations <0.1 μm.

Electron Microscopy

Survey of thin and semi-thick sections up to 200 nm in thickness were done on a JOEL 100C transmission electron microscope operated at 80–100 kv. Sections 0.3–1.0-μm thick were examined using a Phillips 430 electron microscope operated at 200–300 kv.

An Eikonix 1412 camera, capable of 12-bit grey scale readout of a 4,096-pixel linear detector array, was used with a Gordon Model 5 × 5 Plannar light source (Gordon Instruments, Orchard Park, NY) to digitize negatives using software developed in the laboratory for a DEC Microvax 3200. 1,024 × 1,024 areas were scanned, with correction for individual pixel variations in gain and dark current, and flat-fielding correction for variations in light intensity over the area of the light box.

Tilt sets for tomographic reconstruction were acquired on a specially equipped, Phillips 430 electron microscope located in the Howard Hughes Medical Institute EM facility at University of California (San Francisco, CA) (Koster et al., 1992). Stepping motors provide fine motor control of tilt angle and specimen height. A slow scan, Peltier-cooled CCD camera with 1,024 × 1,024 pixels and a 12-bit grey scale readout coupled by fiber optics to a YAG crystal allows direct digital input of images, with high linearity and dynamic range of signal and low geometric distortion. A Gatan high tilt stage allowed tilts as high as ±70°.

To minimize section shrinkage during data collection, sections were preirradiated by exposure to the electron beam for 20 min at an intensity corresponding to roughly 1 OD film density with a 1-s exposure (at a slightly higher magnification than used for data collection). During subsequent data collection, a beam deflection switch was used to limit exposure to the sample between focusing and camera exposures. A 0° projection was taken at the start of data collection, followed by tilting of the specimen to maximum negative tilt. Projections at progressively higher tilt angles then were taken up to the maximum positive tilt, followed by rotation back to 0° and a 0° projection. Tilt sets ranged from −66 to 70–72° in 2° intervals.

Intensity Normalization and Alignment

For images obtained by digitizing negatives using the Eikonix camera, transmittance values were converted to film optical density. 960 × 960-pixel images digitized at 12-bit grey scale resolution directly from the slow scan, CCD camera mounted within the Howard Hughes Medical Institute's Phillips 430 were normalized to correct for variations in dark current and gain of individual pixels (Koster et al., 1992); these values already are linearly proportional to intensity of electrons. A "mass normalization" procedure, to convert film optical density or CCD intensity values to values proportional to the integrated electron scattering cross section, or electron optical density, was carried out as described previously (Belmont et al., 1987).

Alignment of projections from axial tomographic tilt sets used quadratic interpolation; geometric centers of the projected gold bead images were used as fiducial marks for alignment, and a least squares estimator and a conjugate gradient minimization algorithm (Lawrence, 1983) were used to calculate the common tilt axis location, x-y rotation and translation offsets, relative magnification changes, the three-dimensional positions of the gold beads, and potentially the tilt angle. In fact, Monte Carlo calculations using this alignment procedure indicated that the tilt angle accuracy from the goniometer stepping motor exceeded that expected from the minimization procedure; therefore the tilt angles were held fixed to the actual experimental values in our alignments.

A semi-automated bead picking algorithm was developed to facilitate location of the geometric projected centers of the gold beads. Projections were Wiener filtered (Castleman, 1979), with the "signal" power spectrum based on the bead size, to enhance bead-shaped features from the nuclear background. Segmentation of beads was accomplished using a combination of density and local contrast pixel thresholds, median filtering, and area and perimeter feature thresholds. The geometric center was then calculated for each of the final "bead" features.

An automated matching algorithm then identified specific beads in a reference projection with the corresponding beads in a second projection. The algorithm used a comparison of x and y distances of a given bead from other beads in the reference image versus similar position comparisons for an arbitrary bead in the 2nd projection. Deviations in distances parallel to the tilt axis were emphasized, since these distances are invariant with tilt axis. Using these programs most bead positions could be assigned automatically with the exception of a small remaining number of bead positions, particularly at high tilt angle; these positions were measured interactively using the display program PRISM (Chen et al., 1989).

Tomographic Reconstruction

Three-dimensional reconstructions were obtained through a series of two-dimensional axial tomography reconstructions. We used R-weighted back projection (Ramachandran et al., 1971; Belmont et al., 1987) carried out in Fourier space, with the addition of a gaussian roll-off frequency filter.

Image Processing and Display

Computational blurring of EM micrographs to simulate observation by a light microscope was done by convolution, in Fourier space, of the digitized images with the theoretical, in focus, point spread function for a given numerical aperture lens and wavelength (Goodman, 1968).

Rotation of two-dimensional images and three-dimensional reconstructions was accomplished by quadratic interpolation.

A solid model display program was written which used a gradient evaluation, together with simple ray tracing, to calculate a two threshold solid model. Based on the pixel density relative to these two thresholds, a reflectance of zero or one of two finite values was assigned. To eliminate effects due to lower densities at border pixels, the highest density pixel was used within 4 pixels from the first to exceed the lower threshold. The dot product of the gradient with the illumination direction was used to scale the reflected light intensity. Estimation of the local gradient was calculated by approximately local density values within a 5 × 5 × 5-pixel neighborhood by a linear combination of orthonormal polynomial basis functions (Haralick, 1984) and then evaluating the derivative of this polynomial at the center pixel location.

The display program, PRISM (Chen et al., 1989), running on a DEC Microvax 3200 with a Parallax graphics controller was used to display images and view results. Output of figures used a Lasergraphics LFR film recorder to prepare negatives or a Mitsubishi Colorstream printer for direct printing.

Results

An Apparently Continuous Distribution of Lamin B is Visualized by Thin Section Transmission Electron Microscopy

As a means of quickly optimizing fixation and immunostaining protocols, we stained cells as a monolayer and used silver enhancement and light microscopy as our initial assay. Commercially available anti-vimentin antibodies were used as the primary for our first experiments; visualization of the vimentin cytoskeleton in thin, cytoplasmic regions allowed easy assessment of the signal to noise ratio of staining. Use of a 1 nm gold-labeled secondary antibody followed by silver enhancement allowed good penetration of the secondary while providing a sufficiently strong signal for low-magnification observation. Once conditions were optimized for vimentin we then adapted them for our anti-lamin B antibody. This was an immunopurified, rabbit polyclonal anti-

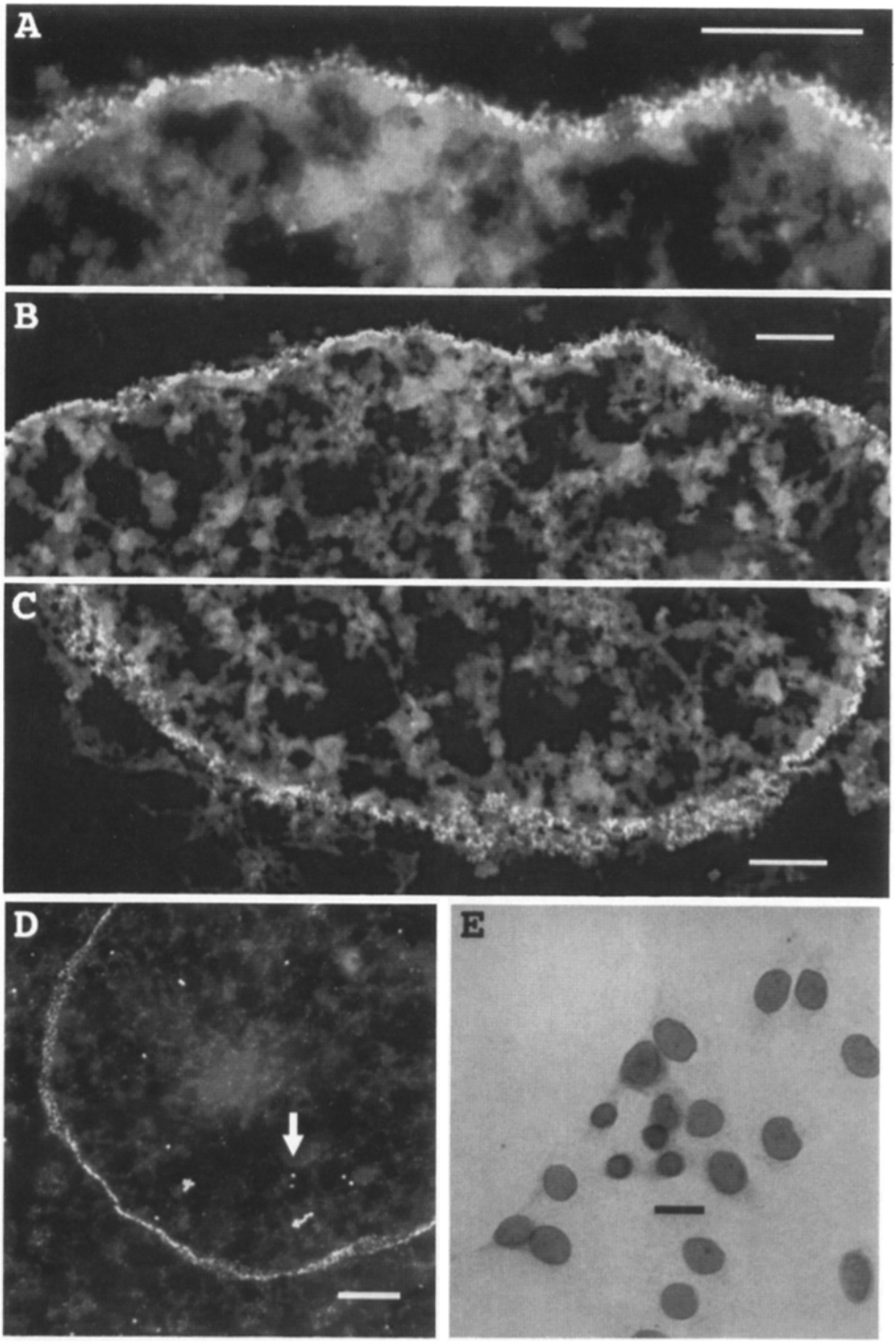

Figure 1. Conventional thin section TEM suggests a continuous lamin distribution: (*a–c*) three different regions of the same CHO nucleus are shown. (*b* and *c*) were contrast enhanced to improve gold visibility at lower magnification. 0.2-μm-thick sections were stained with uranyl and lead salts. Digitized images of micrographs were "mass normalized" (see text) with display similar to a negative—whiter areas correspond to heavier stained regions. Antibody specificity is demonstrated in (*d* and *e*). (*d*) Shows a region of nucleus and surrounding cytoplasm from a 0.45-μm section; heavy staining is seen at the nuclear rim with low level, diffuse background staining over the cytoplasm and nuclear interior. Arrow points to large gold beads added to section for alignment of projections for EM tomography. Very small, grey beads surrounding arrow correspond to individual immunogold, silver amplified beads (~1 pixel in size). (*e*) Shows low power light microscopy image of immunogold stained, Epon embedded cell monolayer; cytoplasmic background staining is very low. Bars: (*a–c*) 0.5 μm; (*d*) 1 μm; (*e*) 10 μm.

body raised against a carboxyl terminus peptide of lamin B (Sobatka-Briner et al., 1992).

Using this approach we were able to achieve a high density of nuclear lamin B staining with low background. The specificity of the antibody used for immunolocalization is illustrated by Fig. 1 *D*, showing a low magnification, transmission electron micrograph of a nuclear region and surrounding cytoplasm from a 0.45-μm-thick section, and by Fig. 1 *E*, showing a low-magnification light micrograph of an immunogold-stained cell monolayer, after Epon embedding. The intense rim of staining at the nuclear periphery visualized in the electron micrograph demonstrates the specificity for the nuclear envelope region while the low cytoplasmic staining is demonstrated by the light micrograph. Control experiments using normal rabbit serum as a primary, or no primary, showed similar cellular background and no above background nuclear staining (data not shown).

Consistent with other recent findings (Bridger et al., 1993), light microscopy revealed some internal staining in a subpopulation of nuclei. By light microscopy only a frac-

tion of these internal staining regions appeared to be the result of nuclear envelope invaginations or internal membrane vesicles. By transmission electron microscopy (TEM)[1], however, most regions of internal staining in fact appeared associated with nuclear envelope; invaginations of the nuclear envelope were either directly visualized, or internal staining was associated with ringlike structures with condensed chromatin tightly apposed to the nucleoplasm side and with an absence of chromatin inside the ring. As demonstrated by stereo-pairs of thick sections visualized by intermediate voltage EM, many nuclei showed prominent invaginations and folding of the nuclear envelope, particularly at the top of the nucleus (side away from the coverslip surface) (data not shown).

EM of sections 0.2 μm in thickness showed nuclear cross-sections with an essentially continuous rim of immunogold labeling as shown in Fig. 1 (*A–C*). Although staining intensity varied along the nuclear perimeter, correspondence with the open network of lamin filaments of lamin filament bundles suggested by previous light microscopy results, as discussed in the Introduction, was not apparent. Thin, 80-nm-thick sections again showed continuous staining but with occasional gaps, presumably due to nuclear pores, and somewhat greater quantitative variations in staining density. It was still unclear to what degree these variations in staining intensity were due to variations in actual lamin surface density versus variations in surface geometry and a resultant variation in density in the two-dimensional projected image.

To test whether the denser islands of staining might correspond to well defined bundles of lamin filaments superimposed on a lower density, more continuous staining pattern, we assembled serial thin section reconstructions. The open network of lamin staining visualized in a previous light microscopy study had suggested spacing of roughly 0.5 μm between network elements, with extension of linear elements for distances up to 1–2 μm in length (Paddy et al., 1990). However, no evidence for such structures were seen in these serial section reconstructions, although the resolution of our alignment procedure was estimated as better than 0.1 μm (data not shown).

An Apparently Open Network Distribution of Lamin B Is Visualized by Light Microscopy

We considered two possibilities in reconciling our observations with previous light microscopy results. First, that the differences were real and a result of using a different cell line and antibody; the previous study used either Hela cells with a polyclonal rabbit antibody recognizing mammalian lamins A, B, and C, or early *Drosophila* embryos and *Drosophila* Kc tissue culture cells with a mouse monoclonal against *Drosophila* lamin. Given the similar appearance described previously for both the *Drosophila* and Hela nuclei we considered this possibility unlikely. Second, that the differences were only apparent and due to resolution differences of light and electron microscopy and the difficulties in subjectively "averaging" immunogold distributions.

We tested this second possibility directly; confocal light microscopy using scattered rather than fluorescent light allowed us to image the sliver enhanced, immunogold labeled nuclei from the very same Epon wafer used to prepare sections for TEM. These confocal light microscopy results, shown in Fig. 2, are now consistent with the previous reports of an "open" network of staining.

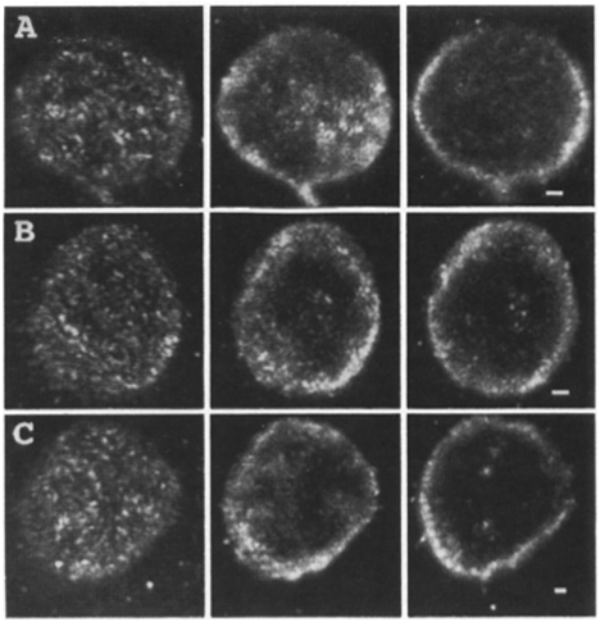

Figure 2. Confocal light microscopy suggests instead a discontinuous, open network of lamin staining: epon-embedded cell monolayers from the same sample preparation used to cut sections shown in Fig. 1 were imaged using scattered light with epi-illumination. (*A–C*) Grazing, top, and mid-sections for three nuclei. Bars, 1 μm.

Light and Electron Microscopy Highlight Consistent but Different Aspects of Lamin B Distribution–Nonuniform Lamin B Distribution over Different Size Scales

We confirmed this consistency between previous light microscopy observations and our own sample preparations by a second method. Semi-thick, 0.5–1.0-μm-thick sections were visualized using an intermediate voltage TEM. Grazing sections of nuclear lamin staining were photographed as stereopairs. After digitization of the electron micrographs, image processing was used to computationally "blur" these images so as to simulate the image degradation produced by a diffraction-limited, ideal light microscope, assuming the entire image to be in focus. This was achieved by convolution of the original EM image with the theoretical point spread function (Goodman, 1968) of an ideal objective lens with a given numerical aperture for a specific illumination wavelength.

The results are illustrated in Figs. 3 and 4. Fig. 3 shows low magnification electron micrographs compared side by side with their simulated light micrographs. The simulated light micrographs highlight an open network with the roughly 0.5 μm spacing characteristic of previous light microscopy studies. Comparison with actual confocal light microscopy (see Fig. 2) and, in particular, results using optical sectioning, deconvolution light microscopy (see Fig. 3 in Paddy et al., 1990, and Fig. 5, this paper) is striking.

Direct comparisons in Figs. 3 and 4 between higher

1. *Abbreviation used in this paper*: TEM, transmission electron microscopy.

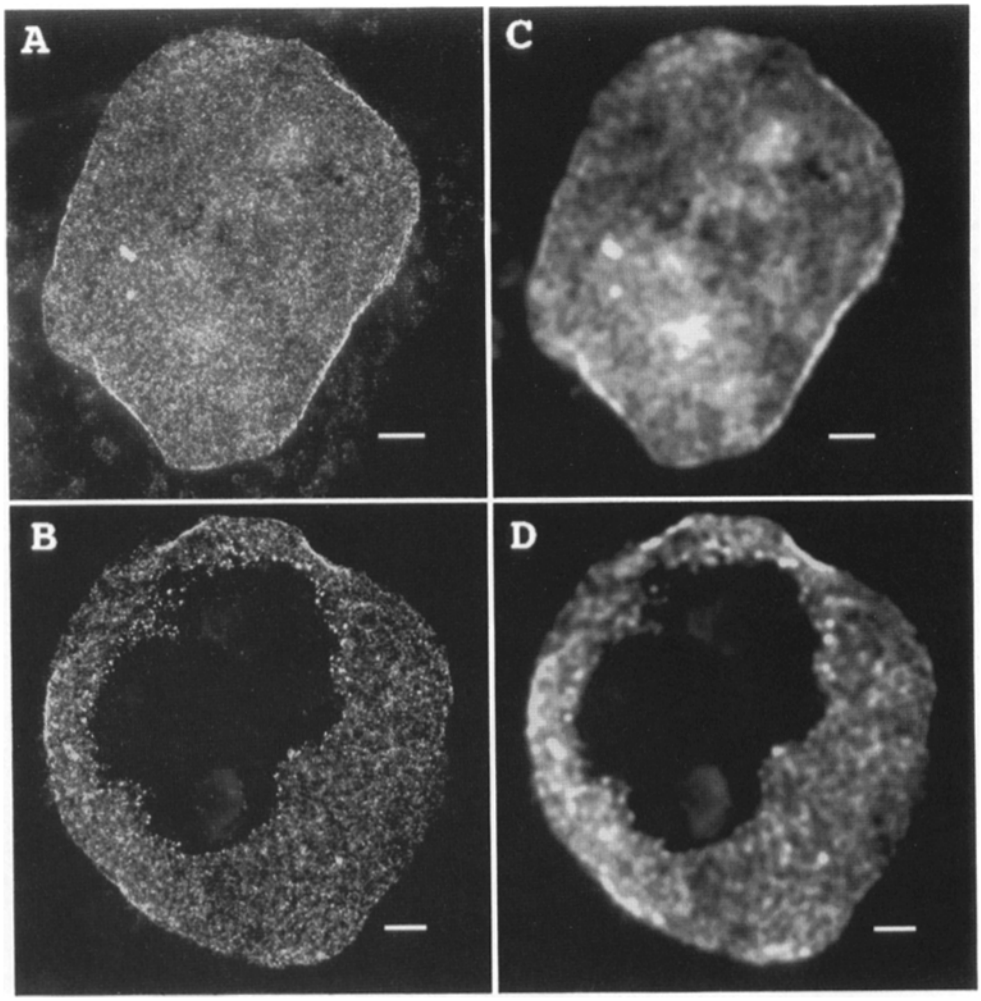

Figure 3. Thin-section TEM and light microscopy highlight consistent but different aspects of lamin B distribution: (*left*, *A* and *B*) 1-μm thick grazing (*A*) or top (*B*) sections of preembedded immunogold labeled nuclei; initial examination suggests random but near continuous distribution of lamin B over the nuclear surface. (*Right*, *C* and *D*) computational "blurring" of images shown in *A* and *B* to stimulate observation of same samples by light microscopy. Images from the left were convolved with a point spread function corresponding to an ideal, 1.3 NA lens imaged with 450 nm light. Now an "open network" similar to that observed by optical sectioning light microscopy is observed. Bars, 1 μm.

magnification electron micrographs and their simulated light micrographs allows identification of the structural features giving rise to the light microscopy resolution network staining pattern. This comparison allows us to exclude the possibility that the apparent fibers visualized by light microscopy correspond to distinct bundles of lamin filaments. What appear as distinct, widely separated fibers at light microscopy resolution at higher resolution are revealed to be part of a more continuous and finer meshwork pattern of lamin staining.

Fig. 4 shows an oblique orientation of a region of the nuclear envelope at higher magnification; a stereo pair from the original electron micrographs in the top panel (best viewed with 2–3× stereoglasses) shows immunogold staining confined to an irregular, convoluted surface which includes a sharp invagination. In the bottom panel are a computationally blurred image simulating the same region visualized by light microscopy and an image representing a blend between the original EM micrograph and the blurred image. Comparison of these images demonstrates several points. First, there is significant lamin staining present in the apparent gaps visualized in the simulated light micrograph. Second, there is obvious heterogeneity in the staining pattern on a smaller, roughly 0.1–0.2-μm scale. Third, the apparent fibers visualized in the simulated light micrograph actually correspond to diffuse regions of heavy staining or the merger of linear, "fiber-like" staining aggregates which have different relative orientations (see below).

Overall the pattern of staining at higher resolution, although heterogeneous and mesh-like, does not suggest any obvious, ordered structure. Due to the still limited resolution of our staining and imaging techniques it is not possible to directly visualize individual lamin filaments. However, several general features can be described which are relevant to results discussed below. It is possible to recognize within this meshwork roughly linear regions of heavier staining about 0.1 μm in width and extending up to 0.5 μm in length (Fig. 4 *a*, *arrows*); these may be related to the observed capping of surface associated chromatin by heavy lamin B staining, discussed below. Also, a number of "holes" completely devoid of immunogold staining are outlined by surrounding stained regions (Figs. 4 *a* and 6 *a*); in light of the roughly 0.1-μm-diam of these holes, it is possible that they correspond to locations of nuclear pores.

Finally, in regions of light staining it is possible to recognize linear "strings" of beads which may represent individual lamin filaments. These are actually best appreciated in the three-dimensional tomographic reconstructions discussed later in this paper where the question of superposition of distant beads in the projected image is not an issue (see Fig. 8,

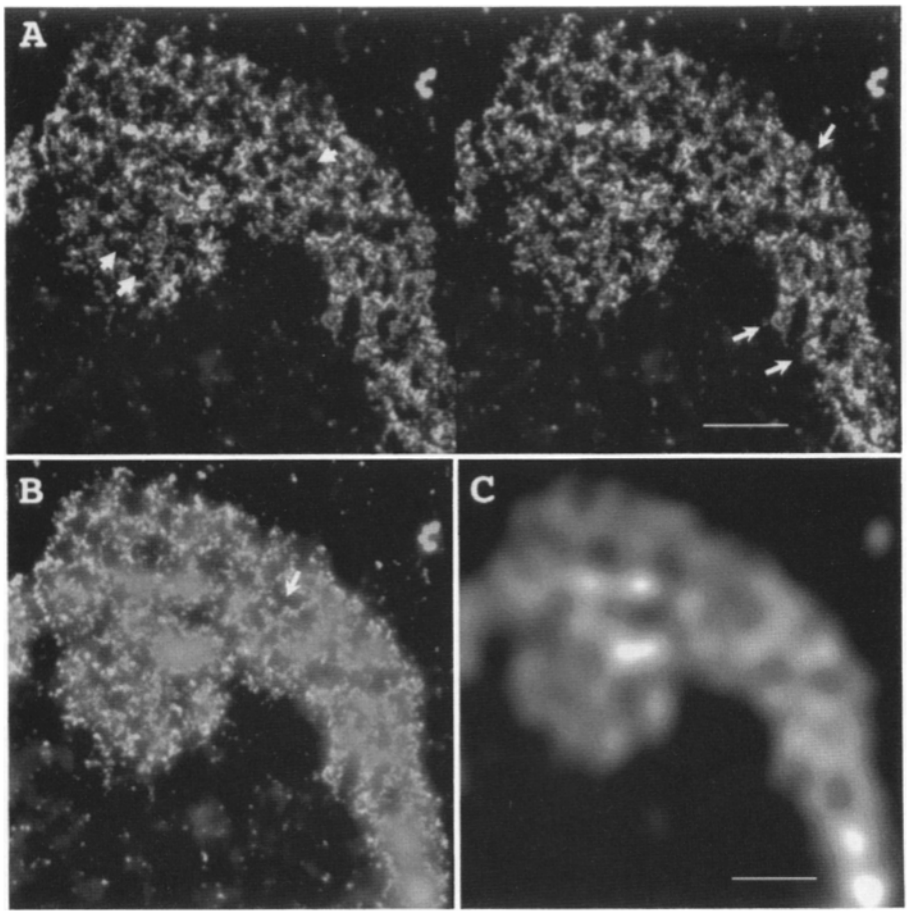

Figure 4. Lamin B spatial distribution is heterogeneous over two different size scales: (*A*) stereopair electron micrograph of oblique, 0.4-μm thick section through nuclear lamina demonstrates considerable heterogeneity in lamin B distribution over a roughly 0.1–0.2 μm scale. Long arrows point to linear, heavily stained regions roughly 50–150 nm in width. Short arrows point to roughly 0.1 um diameter "holes" in immunogold staining which may correspond to locations of nuclear pores (see also Fig. 6 *a*). (*C*) Computationally blurred image of right side of stereo pair shown in *A* simulates observation by light microscopy with a 1.3 NA lens (450-nm wavelength). Variations in overall lamin B staining on roughly a 0.5-μm scale are highlighted. (*B*) Blend of blurred image with original electron micrograph allows easy comparison and shows that the apparent fibers seen at light microscopy resolution do not correspond at higher resolution to distinct, oriented fiber bundles (see text). Bars, 0.5 μm.

A and *B*). Measurements from several such bead arrays yield a mean, three-dimensional bead separation of 6 pixels, which with the pixel size of 4.75 nm translates to 28 nm. This spacing is close to the observed axial repeat of 24.5 nm for lamins A and C (Aebi et al., 1986), consistent with the interpretation that these features represent individual lamin filaments and that the anti-peptide antibody is recognizing a unique site on the lamin molecule.

Nuclear Pore Clusters Are Positioned between Regions of Heavy Lamin Staining

The results presented above demonstrated that the apparent fibrillar staining pattern visualized at low resolution by light microscopy corresponded to quantitative variations in lamin staining rather than actual discrete bundles of lamin filaments. Moreover, 0.1-μm-diam holes, matching the known size of nuclear pores, were visualized in the lamin B staining pattern. Previous work using scanning EM demonstrated that a large fraction of nuclear pores are present as small clusters in mammalian cells (Maul et al., 1972), and previous immunolocalization of lamins in rat liver nuclei indicated that lamins are absent or decreased in density underneath pore complexes (Gerace et al., 1982). Therefore the observed variation in lamin staining over the roughly 0.5-μm scale observed could be related to a reduction of local lamin concentration in regions occupied by clusters of nuclear pores. As a means of addressing this issue, we used a mAb specific for a family of nuclear pore glycoproteins to compare the distribution of nuclear pores and lamin using optical sectioning, fluorescence light microscopy.

A computer controlled, wide-field microscope equipped with motorized filter wheels and focus and a cooled, slow scan CCD camera was used to collect complete through-focus series of entire nuclei from double lamin/nuclear pore stained CHO cells. At each focal plane, FITC (nuclear pore) and Texas red (lamin B) images were acquired; the use of a single, combination dicroic mirror facilitated registration of these images. The focus interval was 0.2 μm and data from 40–60 focal planes was collected for each data set. Out-of-focus blurring was reduced through use of an iterative, constrained deconvolution algorithm.

In consideration of the severalfold lower resolution along the optical axis, even after deconvolution, we focused our comparison of lamin B and nuclear pore staining to projections of the top and bottom nuclear surfaces. A running average of 15 optical sections centered about the top or bottom nuclear surface was computed from the deconvolved reconstructions, corresponding to a 3-μm projection through the top or bottom of the nucleus. Except for the nuclear rim and regions of nuclear envelope invagination, this approach largely eliminated problems related to overlap of fluorescence from regions in a different focal plane due to blurring along the optical axis. It also largely eliminates z axis registration problems, given the large projection volume used.

Fig. 5 shows results from this comparison. Nuclear pore staining (*red*), representing pore clusters and/or individual

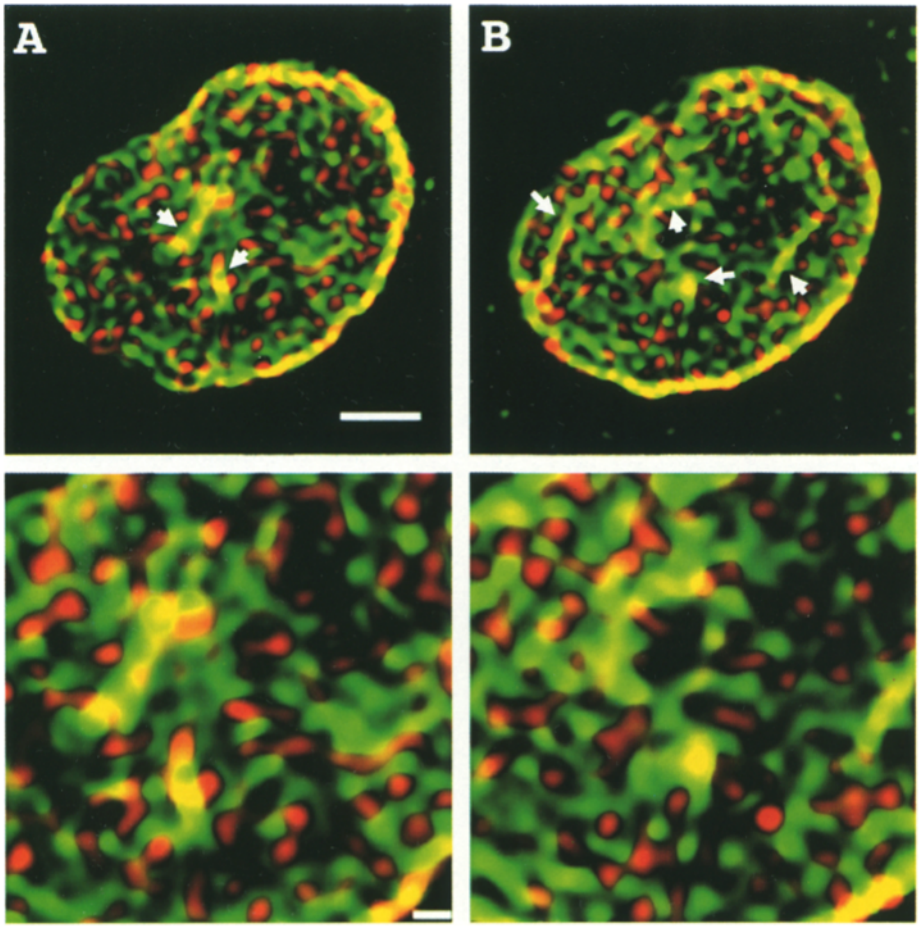

Figure 5. Comparison of lamin and nuclear pore staining by optical sectioning light microscopy. *A* and *B* correspond to the top and bottom of a nucleus respectively. 15 deconvolved optical sections containing the top or bottom of a nucleus were summed to form 3-μm projections. Lamin B staining (*green*) is shown superimposed with pore staining (*red*). Smallest spots are likely individual pores with most pore staining present as larger areas which likely represent pore clusters (see text). Bottom panels contain 2× enlargements of selected regions. Most yellow staining, indicative of lamin/pore colocalization, is confined to the nuclear rim or to a small number of large structures marked by arrows. Based on examination of individual optical sections, these structures appear to be invaginations of nuclear envelope. In both cases, apparent colocalization is likely due to overlap of spatially separate pore and lamin regions in the projection. Outside of these areas, pore staining is concentrated between or adjacent to regions of heavy lamin B staining. Bars: (*top*) 2 μm; (*bottom*) 0.5 μm.

nuclear pores, is concentrated in regions between or adjacent to areas of heavy lamin B staining (*green*). In a number of cases, nuclear pores clustered in short, linear arrays, are visualized adjacent and parallel to linear regions of heavy lamin B staining. Yellow regions, indicating overlap of pore and lamin staining, are confined to the nuclear rim and to a small number of localized structures (Fig. 5, *arrows*) within the projected images. Examination of individual optical sections from the corresponding three-dimensional reconstructions demonstrates that these internal structures showing overlapping of pore and lamin staining correspond to invaginations of the nuclear envelope surface. In both these cases, overlap of pore and lamin staining in the projected image would be expected simply due to the geometry; regions of lamin and pore staining separated in z, the optical axis, would project to the same location in the x-y plane.

Nuclear Envelope–associated Chromatin Underlies Heavy Concentrations of Lamin B

Recently, roughly 120-nm diam large-scale chromatin domains formed by the packing of component 10 and 30 nm chromatin fibers have been identified within interphase nuclei (Belmont et al., 1987, 1989). It was of interest to compare the spatial variations in the lamin B meshwork visualized at higher resolution to the underlying chromatin distribution, particularly given the apparent matching in size of these large-scale chromatin domains to similar size regions of heavy lamin staining.

Semi-thick sections 0.4–0.5 μm in thickness were counterstained with uranyl and lead salts. Attention focused particularly on grazing sections in which the top of bottom of the nuclear envelope was included within the section, or else on mid-nuclear sections in which portions of the nuclear envelope were oriented oblique to the section plane. Alternatively, mid-nuclear sections were imaged at high tilt to produce a similar oblique orientation in which a significant area of the envelope could be projected onto the plane of the micrograph. A correlation between heavier immunogold labeling and large-scale chromatin domains approaching the nuclear envelope surface was suggested (data not shown).

There were two difficulties, however, in this analysis. The degree of silver amplification produced beads roughly 20 nm in size. These beads were difficult to visualize within semi-thick sections at low magnification against the highly stained chromatin regions. Analysis of large nuclear regions was hindered, and therefore the statistical significance of the apparent association was less clear. More importantly, the closeness of association between heavier concentrations of lamin staining and chromatin was difficult or impossible to judge as the images represent projections through a thick sample. As shown earlier, however, thin sections did not reveal the three-dimensional architecture which allows recognition of these regions of heavier labeling.

To overcome these problems we carried out axial tomographic reconstructions on lower magnification, semi-thick sections stained only with uranyl. Lighter staining provided higher contrast between the silver enhanced colloidal gold

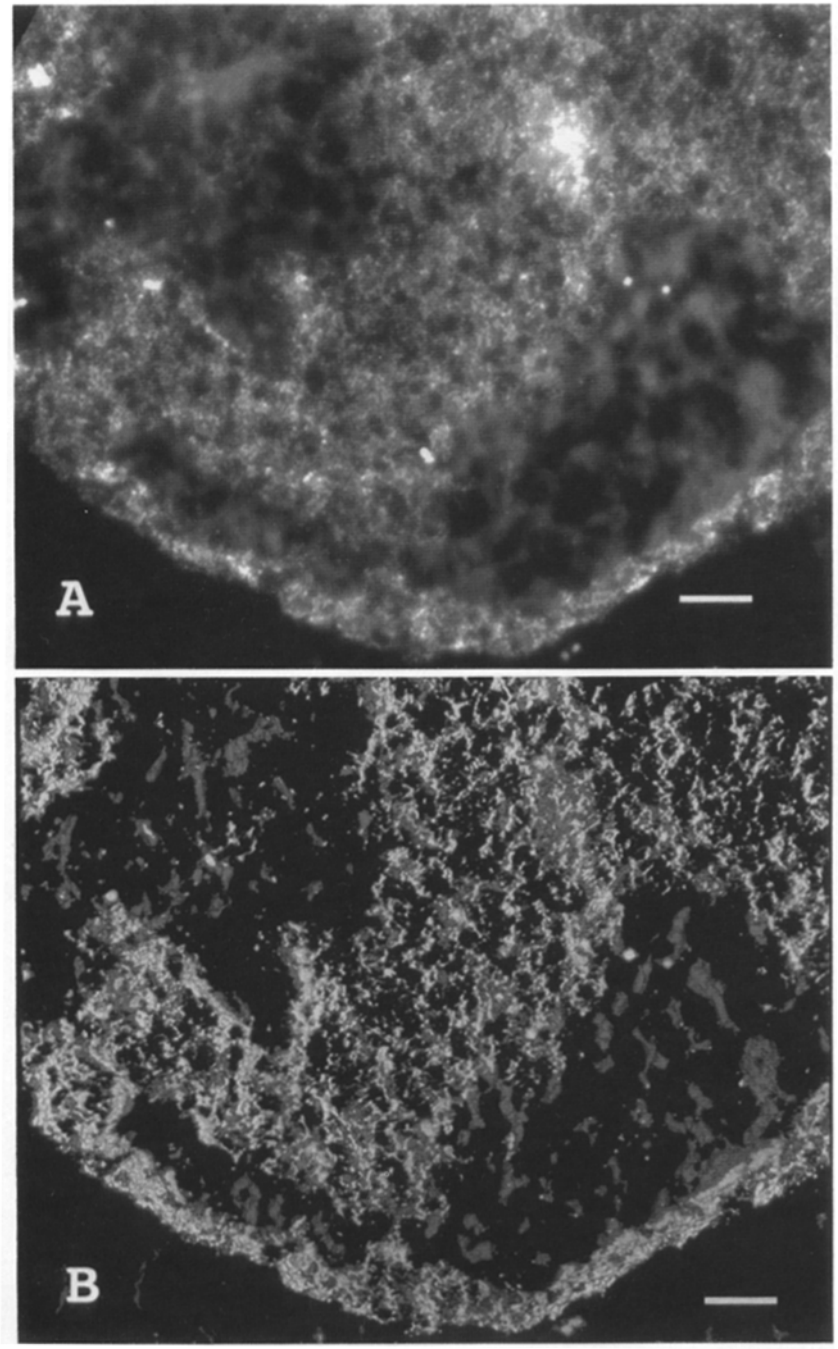

Figure 6. Solid model display of grazing nuclear section highlights close correlation between heavy lamin staining and peripheral chromatin: 0.4-μm thick section which includes top of nucleus over large area stained with uranyl only. (*A*) Original 0° projection, containing central region in which top of nucleus is contained within physical section. Grey staining within nucleus corresponds to chromatin. Arrows point to roughly 0.1-μm-diam "holes" in immunostaining which may correspond to nuclear pores. (*B*) Solid model display calculated from the tomographic reconstruction; viewing and lighting are directed from side of physical section facing the exterior of the nucleus. Therefore peripheral lamin B staining (*white*) blocks underlying chromatin (*grey*). Shading was based on a gradient calculation of local densities (see text). Two thresholds were used to distinguish lamin versus chromatin staining. Bar, 0.5 μm.

and the chromatin, while the three-dimensional tomographic reconstructions allowed measurement of the separation between heavy lamin staining and underlying, peripheral chromatin.

EM axial tomography is analogous to medical CAT scanning in the algorithm used to generate the three-dimensional reconstruction; the three-dimensional reconstruction is computed from a series of two-dimensional projections, at different tilt angles, of a three-dimensional object (Frank, 1992). Previous applications of EM tomography have included studies of chromatin (Olins et al., 1984; Woodcock et al., 1991), chromosome (Belmont et al., 1987; Harauz et al., 1987), RNP (Skoglund et al., 1986; Mehlin et al., 1992), and kinetochore structure (McEwen et al., 1993).

Fig. 6 *A* shows the original zero degree projection of the first sample, a 0.4-μm-thick section through the top of a CHO nucleus. Because the cells have been grown and stained on a plastic coverslip, both the cell and the nucleus are flat, allowing significant amounts of the nuclear envelope to be included within this grazing section. A small region of the nucleus is shown. Peripheral labeling at the nuclear periphery is present in addition to staining over the nuclear interior, representing regions of the top of the nucleus which have been included within this grazing section. This interpretation is confirmed by three-dimensional reconstruction results discussed below.

Fig. 6 *B* shows a solid model, generated from the three-dimensional reconstruction, highlighting the chromatin–

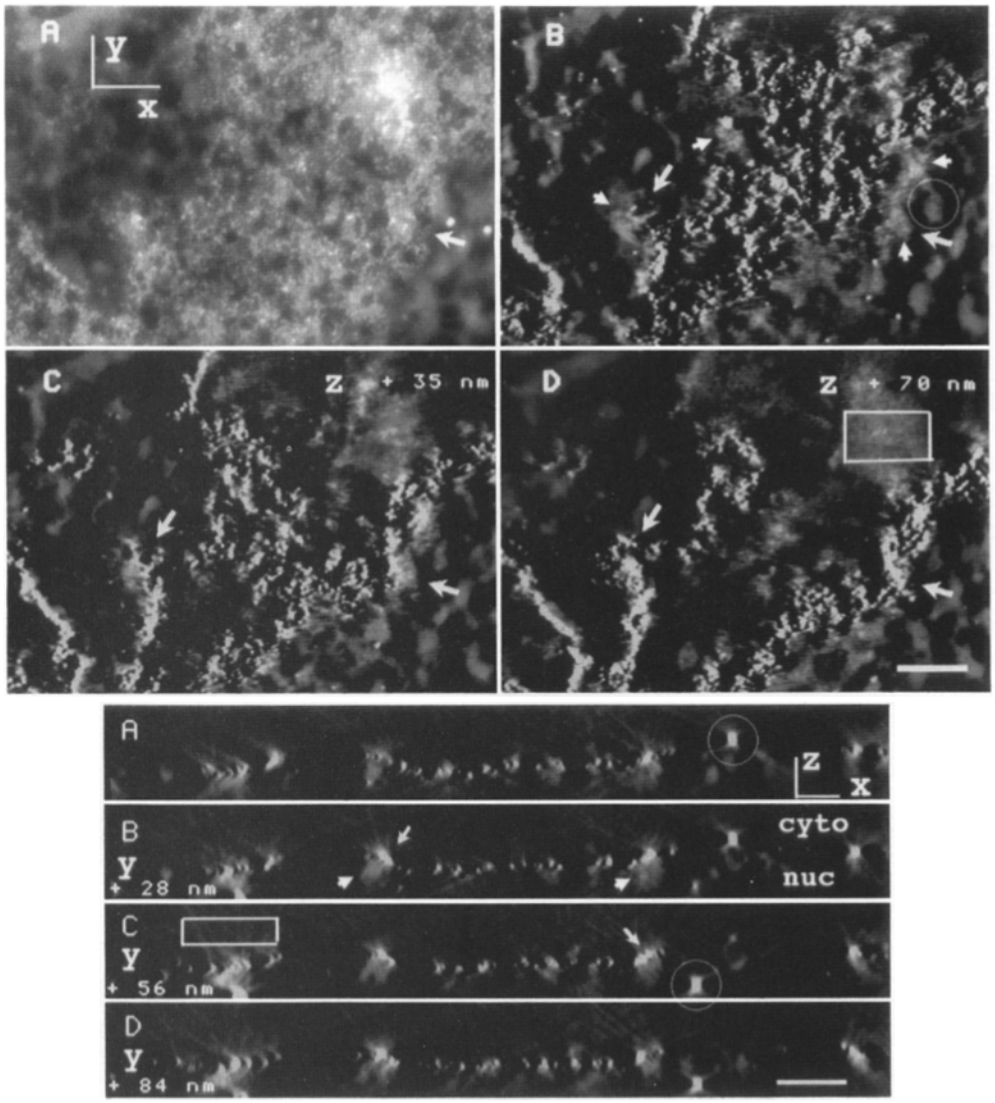

Figure 7. EM tomography confirms close apposition of lamin B staining to peripheral chromatin: Selected regions from the tomographic reconstruction of the grazing nuclear section shown in Fig. 6. (*Top, A*) Subregion of original 0° projection. Projection direction (optical axis) is down z axis, with x-y axes as marked. (*B–D*) Serial slices in the x-y plane, parallel to the actual physical section, computed from the reconstruction. Arrows point to regions demonstrating "capping" of surface associated chromatin by heavy lamin B concentrations. Arrowheads point to lightly stained (*grey*) chromatin regions. Slices in (*B–D*) separated in z direction by 35-nm distance. Circled region shows chromatin region off the actual lamin surface without lamin staining. (Boxed area shows diffuse background, present in regions above the actual physical specimen, due to reconstruction artifacts—see bottom panel (*C*), boxed area); (*Bottom, A–D*) Serial slices from the tomographic reconstruction in the x-z plane, perpendicular to the actual physical section. Each section is separated in y by 28 nm from its neighbor. Top of sections face cytoplasm (*cyto*), bottom of sections the nucleoplasm (*nuc*) with a line of immunogold staining tracing the nuclear lamina. Arrows again point to heavy concentrations of lamin B staining lying directly over and immediately adjacent to peripheral chromatin domains, marked by arrowheads. Circles enclose large gold beads, unrelated to immunostaining, added to surfaces of physical section prior to tomographic reconstruction. (Boxed area above the actual area of the physical specimen contains "rays" which originate from real objects—these are due to reconstruction artifacts.) Bars, 0.5 μm.

lamin correlations. The viewing direction is from the outside of the nucleus, such that any lamin immunogold staining will "cover" underlying chromatin, with views of the lighter shaded chromatin "peeking" through the gaps in the lamin staining. The model highlights the heavy concentrations of lamin staining overlying chromatin, and the general absence of chromatin underlying regions of light lamin staining; however, due to difficulties in defining density thresholds which would uniquely define either the silver enhanced colloidal gold or the underlying chromatin, the solid model is not perfect and has certain "missing" gold or chromatin staining regions.

Fig. 7 shows cross-sections, parallel or perpendicular to the original physical section (x-y plane), through regions of the reconstruction volume. Fig. 7 *A* (*top*) consists of a selected region from the 0° projection and then three consecutive parallel reconstruction slices (x-y), each separated by 35 nm in z. The selected region includes an area in which the nuclear envelope is completely enclosed within the physical section. Chromatin lying near the nuclear envelope surface is seen in the consecutive slices to be overlaid nearly its entire extent by dense lamin staining; conversely chromatin lying near the surface but offset slightly in distance is not overlaid by heavy staining. Fig. 7 (*bottom*) shows x-z slices perpendicular to the actual physical section plane and more clearly demonstrates this "capping" of heavy lamin staining immediately adjacent to the nuclear envelope facing side of the chromatin domains.

Results from a second sample are shown in Fig. 8. This time a peripheral nuclear envelope region, oriented obliquely to the section plane was chosen. Fig. 8 *A* shows the original 0° projection of the 0.4-μm-thick section. Fig. 8 (*B* and *C*) show selected regions of this projection and corresponding three-dimensional reconstruction slices. To facilitate analysis of the three-dimensional structures giving rise to specific features in the original projection, a single coor-

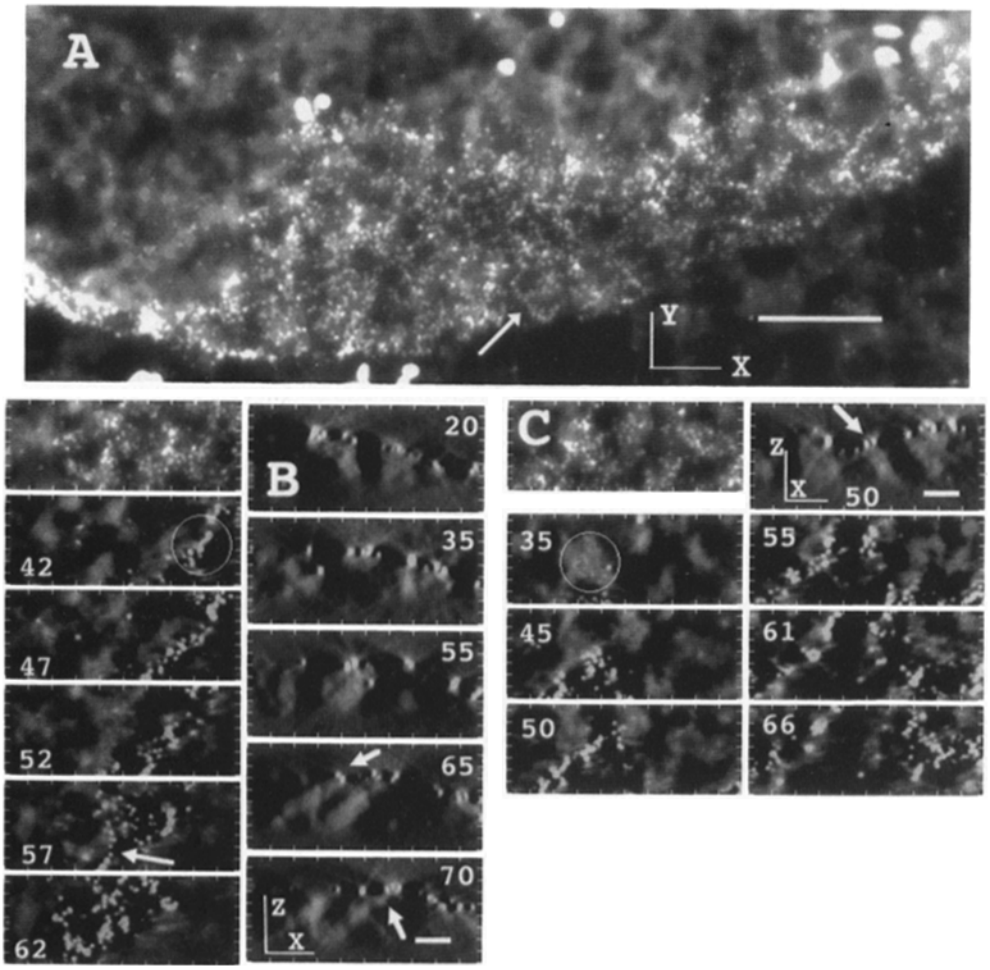

Figure 8. EM tomographic reconstruction of oblique nuclear section–further documentation of peripheral chromatin–lamin correlation: (*A*) original 0° projection of obliquely oriented nuclear envelope region from a 0.4-μm-thick mid nuclear section. Projection direction (optical axis) is down z axis, with x-y axes as marked. Arrow points to "string" of regularly spaced immunogold beads possibly corresponding to staining of a single lamin filament (see text); similar "string" marked in reconstruction slice by large arrow, (*B*) left panel. (*B* and *C*) Selected regions from projection shown together with selected slices from the computed three-dimensional reconstruction. Grid marks on images allow comparison of specific features from projection with corresponding regions from the reconstruction–displayed as x-y slices parallel to the original physical section or x-z slices perpendicular to the physical section. Spacing is 20 pixels for horizontal marks and 10 pixels for vertical marks (1 pixel = 4.75 nm). (*B*) Top left panel, 0° projection; bottom left images = x-y reconstruction slices with z depth indicated by numbers; right panel = x-z slices with y values indicated by numbers. (*C*) Top left panel, 0 degree projection; bottom six images, left and right = x-y slices with z depth indicated by numbers; top right = x-z slice at y = 50. Circles show obliquely oriented lamina regions; absence of lamin staining over chromatin in top left area of circle (*C*) due to chromatin being inside nucleus. Other areas show attachment of chromatin to lamin staining. Short arrows (*B* and *C*) show "capping" of surface associated chromatin by lamin; due to diagonal orientation of chromatin domains, correlation of lamin and surface associated chromatin is much stronger as analyzed in x-z reconstruction slices than indicated by original projection. Bars: (*A*) 0.5 μm; (*B* and *C*) 142 nm.

dinate system was used for all images; the x-y plane corresponds to the plane of the original physical section with the microscope optical axis and projection direction corresponding to the z axis. Parallel reconstruction slices in the x-y plane are shown at stated z depths, and x-z perpendicular slices at stated y positions. Grid marks allow cross-reference between the projection and orthogonal reconstruction slices.

Close examination of these figures demonstrates a strong correlation between heavy lamin staining and chromatin regions immediately adjacent to the nuclear lamina which is strengthened by the reconstruction results: in the projection, a number of areas of peripheral chromatin apparently are overlaid by intense but irregularly distributed lamin staining. In the reconstruction slices, however, many of these peripheral chromatin regions are visualized as lying oblique to the z axis with only a fraction of their area actually directly apposed to the nuclear envelope; those sites attached are nearly all "capped" by lamin staining. In contrast, contiguous chromatin areas slightly offset from the nuclear envelope correspond to areas in the projection with reduced or no lamin staining overlying the underlying chromatin. Similarly, other chromatin regions without overlying lamin staining can be demonstrated in the reconstruction slices as corresponding to chromatin lying some distance off the nuclear envelope (data not shown).

Prophase Lamin B Distribution Resembles Interphase Distribution and Is Not Restricted to Areas Overlaying Condensed Chromosomes

A trivial explanation of the observed "capping" of nuclear envelope associated chromatin by heavy lamin staining would be simply that any lamin B not stabilized by interaction with surface associated chromatin is solubilized during the immunostaining protocol. Our observed lamin B distribution therefore would reflect this selective stabilization of lamin B by chromatin rather than the actual lamin B distribution over the nuclear envelope in vivo. This explanation would appear unlikely based on the known resistance of lamins to detergent extraction. However, a more direct argu-

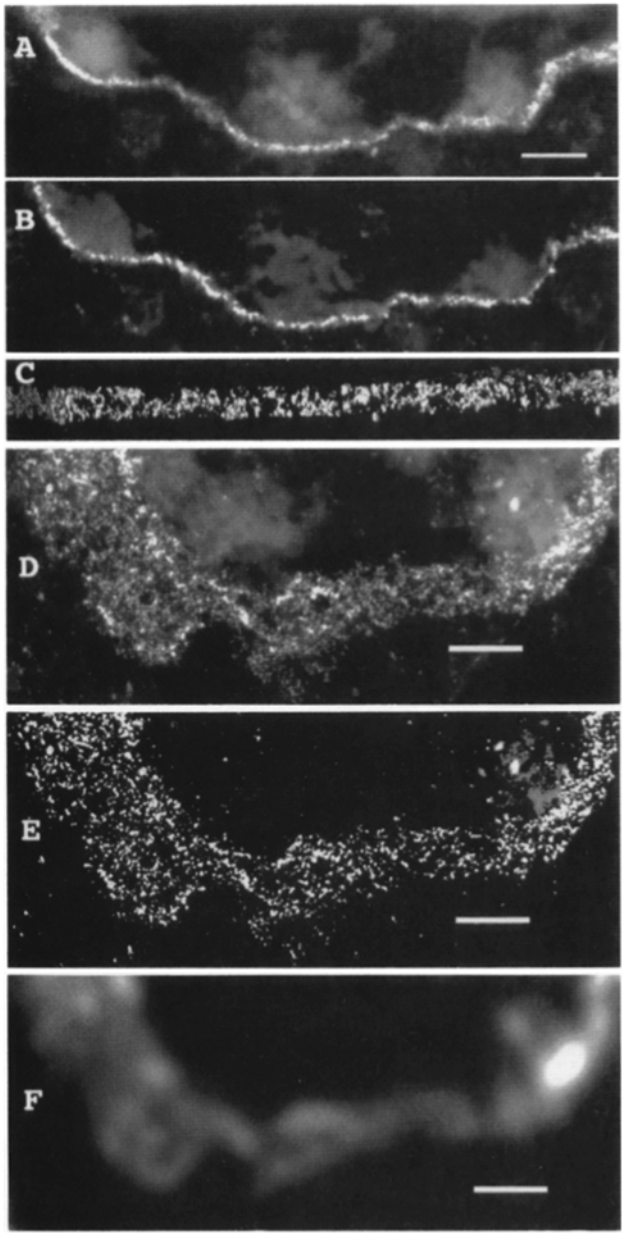

Figure 9. Prophase nucleus shows similar lamin B distribution over chromatin free regions of the nuclear envelope: (*A*) region from 0° projection of mid-nuclear, 0.4-μm thick section through prophase nucleus. Note widely spaced condensed chromatids adjacent to the nuclear envelope. (*B*) Computational slice parallel to the physical section from tomographic reconstruction of the same region shown above. (*C*) Solid model of lamin staining computed from reconstruction showing end-on view, perpendicular to the slice in *B*. Viewing direction is along the vertical axis in *A* and *B*. (*D*) 0° projection of an obliquely oriented nuclear envelope region, photographed from a 0.4-μm-thick serial section several microns removed, but from the same prophase nucleus, as that shown in *A–C*. (*E*) Immunogold staining pattern, largely separated from chromosomal staining through a combination of local contrast enhancement and density thresholding. (*F*) Simulation of image (*E*) as observed in light microscope with 1.3 NA lens and 450 nm light. Note the similar staining pattern to that observed for interphase nuclei, with no increase in concentration adjacent to condensed chromatids. Also, the computational blurring shown in *F* highlights a quantitative variation in lamin staining over a roughly 0.5-μm size scale similar to that seen in interphase nuclei. *A–C* and *D–F* are at the same magnifications. Bars, 0.5 μm.

ment against this explanation is the observed staining pattern for a prophase nucleus, illustrated in Fig. 9.

A low magnification, 0° projection of a mid-nuclear, 0.4-μm-thick section through this prophase nucleus shows a rim of lamin staining circling the nucleus whereas the surface associated chromatin is confined to condensed chromosomes well separated along the nuclear periphery. Tomographic reconstruction of a small region from this nucleus reveals a lamin B network with no increased staining near the condensed chromosomes. A 0° projection of a different 0.4-μm-thick section from the same prophase nucleus shows an obliquely sectioned nuclear envelope region with similar staining pattern as visualized earlier for interphase nuclei (see Figs. 3 and 4) and again with no overall staining variation near the envelope-associated, condensed chromosomes.

The lamin B distribution therefore is stable to our immunostaining conditions independent of any interaction with chromatin. Close examination of the immunogold staining distribution also suggests a similar quantitative variation in staining intensity on a roughly 0.5-μm size scale to that observed for interphase nuclei. This is highlighted by the computational blurring of the obliquely sectioned prophase nuclear envelope region in Fig. 9 to simulate the appearance which would be observed at light microscope resolution. A local contrast enhancement procedure (as used in Fig. 1) together with a truncation of all density values less than a given density was used to isolate the immunogold distribution from most of the chromosomal staining prior to blurring. (A similar pattern over the nuclear envelope region is seen if the original image is used, however, the contrast is slightly reduced presumably due to contributions from chromosomal and other staining; data not shown.)

These results therefore also suggest that the lamin B distribution does not change significantly during prophase chromosome condensation.

Discussion

In summary, this paper describes a three-dimensional ultrastructural analysis, at ~20 nm resolution, of the distribution of lamin B over the nuclear envelope in CHO cells. A complex pattern of lamin B distribution is revealed and a direct structural association between lamin B and peripheral chromatin is demonstrated. The nearly 1:1 relationship between heavy concentrations of lamin staining and underlying, surface associated chromatin argues strongly for the nuclear lamina providing a key structural role in the organization of interphase chromosome architecture.

Two features of lamin B organization are prominent. On a 100–200 nm scale, lamin B staining is organized in a heterogeneous, meshlike pattern without any obvious, ordered structure. Linear regions of heavier staining ranging from 0.05–0.15 μm in width and extending up to 0.5 μm in length can be recognized; these regions correspond largely to confinement of intense staining to areas which directly parallel and overlay nuclear envelope associated, large-scale chromatin domains. Tomographic reconstructions demonstrate the "capping" of lamin B over these surface associated chromatin regions. Lamin B staining, within the roughly 20 nm resolution of our staining techniques, is directly apposed to the nuclear envelope surface of the chromatin. Thinner, linear staining patterns, which may correspond to individual

lamin filaments, and more diffuse staining regions are also present. In certain locations, "holes" completely devoid of immunogold staining are outlined by surrounding stained regions; given the roughly 0.1-μm diam of these holes, it is likely that they correspond to locations of nuclear pores.

On a larger scale, there is a significant quantitative variation in lamin B staining. At lower resolution, including light microscopy observations, this gives rise to apparent "fibers" separated by 0.4–0.5 μm. These apparent "fibers" actually correspond at higher resolution to diffuse regions of heavy staining or the merger of linear regions of heavy staining, described above, which have different relative orientations. Between these apparent "fibers" lamin B staining is present at lower density. Colocalization of nuclear pore and lamin staining by light microscopy shows that clusters of nuclear pores fall largely between or adjacent to the apparent "fibers" of lamin B staining, within the regions of lower lamin B density.

As discussed further below, the combination of increased lamin B staining capping surface associated, large-scale chromatin domains and decreased average lamin B staining in regions of pore complexes may explain much of the observed heterogeneity in lamin B distribution at this level of resolution.

Relationship to Earlier Studies

As described in the Introduction, previous structural studies examining the distribution of lamins over the nuclear envelope yielded apparently contradictory results. In *Xenopus* oocytes, a textile-like orthogonal patterning of closely spaced filaments was observed, with 50 nm spacing between filaments (Aebi et al., 1986). Postembedding immunogold staining of rat liver nuclear lamina preparations indicated a continuous distribution of lamin staining, with the exception of gaps presumed to be due to pore complexes or statistical fluctuations in immunogold staining. The most straightforward interpretation of these results was that lamin distribution in somatic, diploid nuclei was similar to the tightly packed, highly ordered network described for the *Xenopus* oocyte lamina. In contrast, the most straightforward explanation of previous light microscopy results was that the lamina of mammalian somatic and *Drosophila* embryonic nuclei was in fact composed of distinct, widely separated bundles of lamin filaments. Preliminary immunogold staining of *Drosophila* embryonic nuclei supported this conclusion in showing widely spaced islands or fiberlike staining regions.

The lamin distribution we observe in mammalian somatic nuclei cells differs from the observed lamina structure described for *Xenopus* oocyte nuclei. However, it is consistent with both previous EM results for mammalian somatic nuclei (Gerace et al., 1978; Gerace et al., 1981) and light microscopy results for embryonic and somatic *Drosophila* mammalian somatic nuclei (Paddy et al., 1990).

Specifically, using the very same sample preparation we showed that by traditional thin-section TEM an apparent continuous staining distribution around the nuclear rim was observed with no clear evidence of a difference of lamin distribution overlying surface associated chromatin. In contrast, at lower resolution an apparent open network similar to that previously described by fluorescence optical sectioning light microscopy was visualized. This was observed by direct confocal light microscopy using scattered light from the immunogold stained sample, by wide-field fluorescence light microscopy followed by deconvolution, and by computational blurring of thick-section electron micrographs to simulate observation of the same samples by an ideal light microscope.

Only the combination of three-dimensional visualization methods applied to thick sections viewed by TEM allowed the actual, more complex lamin B distribution to be appreciated while also reconciling the previous light and electron microscopy studies. It was also the application of these visualization methods which provided a clear demonstration of the close association between lamin B and chromatin.

This association had been missed in previous TEM studies largely due to limitations of conventional thin section TEM in imaging three-dimensional cellular structure. The variations in lamin staining and chromatin distribution occur on a three-dimensional surface over a 0.1–0.5-μm size scale. thin sections, typically 0.05–0.1-μm thick and viewed in projection, cannot reveal the spatial organization of the quantitative variations in lamin staining over this larger size scale. Similarly, we attribute the differences between our observations and earlier conclusions based on light microscopy optical sectioning as due primarily to technical considerations. In this previous work (Paddy et al., 1990), a clear correlation between lamin and DNA staining was observed with 65% of the most peripheral chromatin loci aligned with only a small angular offset with the lamin network. However, because the lamin and DNA intensity peaks were separated by roughly a 0.2-μm distance, the possibility of an intermediate, bridging protein complex was suggested as linking the nuclear lamina and chromatin.

In this case, the resolution limitations of optical microscopy (roughly 0.25 μm perpendicular to the optical axis and 0.75 μm parallel to the optical axis) limit the importance of such statistical comparisons. For example, in Fig. 1 it is clear that a significant fraction of the chromatin within a 0.25-μm distance of the nuclear lamina is offset from the nuclear envelope. Many of these offset regions would represent peaks of DNA staining in the light microscope, even though the overlying lamina is immediately adjacent to smaller regions of surface associated chromatin. We suggest that the previously observed offset from the nuclear envelope represents segments of decondensed interphase chromosomes looping away from contiguous chromosome segments which are physically attached to the envelope through interactions with the nuclear lamina; this would explain the observed rotational alignment of peaks of DAPI staining with heavy lamin staining.

Our results still differ from the preliminary EM results reported for lamin staining in *Drosophila* early blastoderm embryos (Paddy et al., 1990). It is possible that the lamin organization of these rapidly dividing, early blastoderm nuclei is different from somatic mammalian cells. This might be related, for instance, to a difference in the number of nuclear pores or in the large-scale chromatin organization. However, by light microscopy no obvious difference was observed. We presently attribute the more discontinuous pattern observed by TEM in this previous study to the very low overall immunogold staining density achieved (followed by high silver amplification of what gold beads were present). This was likely a combined result of nonoptimal immunostaining conditions and reduced accessibility to the gold secondary antibodies, due to different fixation conditions and/or

differences in the actual size of the particular gold labeled secondary antibodies used.

Biological Implications

The most interesting observation of our studies is the intimate association observed between lamin B staining and nuclear envelope associated chromatin. Although nuclear lamins were suggested as playing a key structural role in anchoring chromosomes to the nuclear envelope from the time they were first identified, this suggestion was based initially on the known tight apposition of peripheral chromatin against the nuclear envelope and the speculation that this association was mediated through interactions with the nuclear lamins. As summarized in the Introduction, more recent biochemical and genetic data have provided actual evidence for interactions between lamins and chromatin and/or DNA. Our data showing a "capping" of heavy lamin B concentrations directly over surface-associated chromatin domains provide the strongest structural evidence to date for lamin/chromatin interactions within native nuclei.

The resolution of our immunostaining techniques is on the order of 20 nm, due to the 9 nm size of primary and secondary antibodies. Our results therefore do not distinguish between a direct lamin–chromatin interaction versus an indirect interaction through a bridging protein or protein complex. However, they are consistent with models of direct lamin interactions with chromatin or DNA MAR sequences (Glass et al., 1990; Luderus et al., 1992), and make unnecessary models which require bridging complexes extending over distances as large as 200 nm (Paddy et al., 1990).

Perhaps the most interesting aspect of our results is not the association per se of lamin B and surface associated chromatin, but the actual degree of coalignment of heavy lamin staining and the underlying large-scale chromatin domains. A recent study demonstrated that intact mitotic chromosomes lowered the critical concentration of lamin polymerization (Glass et al., 1990). Our results for interphase nuclei are consistent with a model in which large-scale chromatin domains serve as nucleation sites for lamin filament formation, leading to higher concentrations of lamin overlying regions of peripheral chromatin. Our results also lead us to speculate that the lamin network is dynamic over a time scale of hours; while the coalignment of lamin and chromatin was observed in all interphase nuclei from a log phase population, chromatin distribution within the nucleus is cell cycle dependent.

Finally, our results substantiate a nonuniform quantitative variation in lamin distribution over a roughly 0.5-μm size scale. We find this variation is correlated with the nuclear pore distribution, with nuclear pore clusters and/or individual nuclear pores localized adjacent or between the apparent "fibers" of heavy lamin B staining visualized by light microscopy. A simple explanation of this variation in lamin B staining at low resolution would be that the regions of high lamin B staining merely reflect areas of the nuclear envelope lying between clusters of nuclear pores; with areas underlying nuclear pores excluding nuclear lamins, a more or less uniform lamin B distribution would lead to low lamin B staining over regions containing nuclear pore clusters based on the fractional area occupied by nuclear pores. However, because the observed nuclear pore staining does not completely fill the areas of lower lamin staining and because some regions of lower lamin staining also have low pore staining, a second possibility is also possible. Namely that the observed anti-correlation of lamin and nuclear pore staining in fact reflects a differentiation of the nuclear envelope into regions of different lamin organization which correlate with different nuclear pore densities. Higher resolution, double-label EM studies will be needed to distinguish between these possibilities.

Our current hypothesis is that the observed lamin B and nuclear pore distribution are both manifestations of a more global nuclear organization which includes the intranuclear distribution of interphase chromatids. We postulate that interphase chromatids, although decondensed, are still maintained in local, chromosome domains which interact with the nuclear envelope. Capping of 0.05–0.15-μm-diam large-scale chromatin fibers by high concentrations of lamin B would lead at lower resolution to regions of high lamin B staining due to the clustering of these individual large-scale chromatin domains within larger chromosome domains. Insertion of nuclear pores may then be directed to regions between these chromosome domains, creating chromatin-free "channels" extending into the nucleus.

Future Directions

Using the three-dimensional visualization approaches described in this paper, we were able to identify new aspects of lamin distribution and lamin/chromatin interactions which had previously been missed by conventional light and electron microscopy approaches. Using similar approaches it should be possible to address questions raised above concerning possible dynamic behavior of the nuclear lamina during the cell cycle, nucleation of lamin polymerization by surface associated chromatin, cell type specific variations in lamin distribution, as well as additional aspects of nuclear lamina architecture. Our results also serve as a model system demonstrating the potential for these EM reconstruction techniques to investigate other aspects of nuclear architecture, such as analysis of the structural organization of potential nuclear scaffolding proteins within native nuclei.

We thank Dr. Dan Chelsky (Dupont) for his gift of affinity purified, anti-lamin B antibody, Drs. David Agard and John Sedat (University of California, San Francisco) for use of their specially equipped Phillips 430 EM for tomography data collection and distribution of the visualization program "PRISM" and the data collection program "Resolve 3D," and Dr. Murray Gibson (University of Illinois, Champaign-Urbana, IL) for use of his Phillips 430 EM. We also thank Dr. Larry Gerace (Scripps Institute) for suggesting the pore/lamin colocalization experiment and providing his RL1 pore antibody. (Confocal microscopy was performed at the Optical Visualization Laboratory, Beckman Institute, and conventional TEM at the Center for Electron Microscopy, both at the University of Illinois, Champaign-Urbana, IL.)

This work was supported by National Institutes of Health grant R29 GM-42516 and a Whitaker Foundation grant, both to Andrew S. Belmont.

Received for publication 25 February 1993 and in revised form 23 September 1993.

References

Aebi, U., J. B. Cohn, J. Buhle, and L. Gerace. 1986. The nuclear lamina is a meshwork of intermediate type filaments. *Nature (Lond.).* 323:560–564.

Agard, D. A., Y. Hiraoka, P. Shaw, and J. W. Sedat. 1989. Fluorescence microscopy in three dimensions. *Methods Cell Biol.* 30:353–377.

Belmont, A. S., J. W. Sedat, and D. A. Agard. 1987. A three-dimensional ap-

proach to mitotic chromosome structure: evidence for a complex hierarchical organization. *J. Cell Biol.* 105:77–92.

Belmont, A. S., M. B. Braunfeld, J. W. Sedat, and D. A. Agard. 1989. Large-scale chromatin structural domains within mitotic and interphase chromosomes in vivo and in vitro. *Chromosoma.* 98:129–143.

Benavente, R., and G. Krohne. 1987. Involvement of lamins in post-mitotic reorganization of chromatin as demonstrated by microinjection of lamin antibodies. *J. Cell Biol.* 103:1847–1854.

Burke, B. 1990. On the cell-free association of lamins A and C with metaphase chromosomes. *Exp. Cell Res.* 186:169–176.

Burke, B., and L. Gerace. 1986. A cell free system to study reassembly of the nuclear envelope at the end of mitosis. *Cell.* 44:639–652.

Castleman, K. R. 1979. Digital Image Processing. Prentice-Hall, Englewood Cliffs, NJ. 205–210.

Chen, H., J. W. Sedat, and D. A. Agard. 1989. Manipulation, display, and analysis of three-dimensional images. *In* The Handbook of Biological Confocal Microscopy. IMR Press, Madison, WI. 127–135.

Dancher, G. 1981. Localization of gold in biological tissue. A photochemical method for light and electron microscopy. *Histochemistry.* 71:81–88.

Fisher, P. A. 1989. Chromosomes and chromatin structure: the extra-chromosomal karyskeleton. *Curr. Opin. Cell Biol.* 1:447–453.

Fisher, D. Z., N. Chaudhary, and G. Blobel. 1986. cDNA sequencing of nuclear lamins A and C reveals primary and secondary structural homology to intermediate filament proteins. *Proc. Natl. Acad. Sci. USA.* 83:6450–6454.

Frank, J. 1992. Introduction: principles of electron tomography. *In* Electron Tomography. Plenum Publishing Corp., New York. 1–13.

Gerace, L., and G. Blobel. 1980. The nuclear envelope is reversibly depolymerized during mitosis. *Cell.* 19:277–287.

Gerace, L., and G. Blobel. 1981. Nuclear lamina and the structural organization of the nuclear envelope. *Cold Spring Harbor Symp.* 46:967–977.

Gerace, L., and B. Burke. 1988. Functional organization of the nuclear envelope. *Annu. Rev. Cell Biol.* 4:335–374.

Gerace, L., A. Blum, and G. Blobel. 1978. Immunocytochemical localization of the major polypeptides of the nuclear pore complex-lamina fraction. *J. Cell Biol.* 79:546–566.

Giloh, H., and J. W. Sedat. 1982. Fluorescence microscopy: Reduced photobleaching of rhodamine and fluorescein protein conjugates by n-propyl-gallate. *Science (Wash. DC).* 217:1252–1255.

Glass, J. R., and L. Gerace. 1990. Lamins A and C bind and assemble at the surface of mitotic chromosomes. *J. Cell Biol.* 111:1047–1057.

Goodman, J. W. 1968. Introduction to Fourier Optics. McGraw-Hill Book Company, San Francisco. 120 pp.

Gruenbaum, Y., Y. Landesman, B. Drees, J. W. Bare, H. Saumweber, M. Paddy, J. W. Sedat, D. E. Smith, B. M. Brenton, and P. A. Fisher. 1988. *Drosophila* nuclear lamin precursor Dm0 is translated from either of two developmentally regulated mRNA species apparently encoded by a single gene. *J. Cell Biol.* 106:585–596.

Haralick, R. M. 1984. Digital step edges from zero crossing of second directional derivatives. *IEEE Trans. PMAI.* 6:56–68.

Harauz, G., L. Borland, G. F. Bahr, E. Zeitler, and M. van Heel. 1987. Three-dimensional reconstruction of a human metaphase chromosome from electron micrographs. *Chromosoma.* 95:366–374.

Hiraoka, Y., J. R. Swedlow, M. R. Paddy, D. A. Agard, and J. W. Sedat. 1991. Three-dimensional multiple-wavelength fluorescence microscopy for the structural analysis of biological phenomena. *Semin. Cell Biol.* 2: 153–165.

Hoger, T. H., G. Krohne, and J. A. Kleinschmidt. 1991. Interaction of Xenopus lamins A and LII with chromatin in vitro mediated by a sequence element in the carboxy terminal domain. *Exp. Cell Res.* 197:280–289.

Koster, A. J., H. Chen, J. W. Sedat, and D. A. Agard. 1992. Automated microscopy for electron tomography. *Ultramicroscopy.* 46:207–227.

Lawrence, M. C. 1983. Alignment of images for three-dimensional reconstruction of non-periodic objects. *Electron Microsc. Soc. South Afr. Proc.* 13:19–20.

Luderus, M. E. E., A. de Graaf, E. Mattia, J. L. den Blaauwen, M. A. Grande, L. de Jong, and R. van Driel. 1992. Binding of matrix attachment regions to lamin B1. *Cell.* 70:949–959.

McEwen, B. F., J. T. Arena, J. Frank, and C. L. Rieder. 1993. Structure of the colcemid-treated PtK1 kinetochore outer plate as determined by high voltage electron microscopic tomography. *J. Cell Biol.* 120:301–312.

McKeon, F. 1991. Nuclear lamin proteins: domains required for nuclear targeting, assembly, and cell-cycle-regulated dynamics. *Curr. Opin. Cell Biol.* 3:82–86.

McKeon, F. D., M. W. Kirschner, and D. Caput. 1986. Homologies in both primary and secondary structure between nuclear envelope and intermediate filament proteins. *Nature (Lond.).* 319:463–468.

Mehlin, H., B. Daneholt, and U. Skoglund. 1992. Translocation of a specific premessenger ribonucleoprotein particle through the nuclear pore studied with electron microscope tomography. *Cell.* 69:605–613.

Newport, J. W., and D. J. Forbes. 1987. The nucleus: structure, function, and dynamics. *Annu. Rev. Biochem.* 56:535–565.

Nigg, E. A. 1989. The nuclear envelope. *Curr. Opin. Cell Biol.* 1:435–440.

Nigg, E. R. 1992. Assembly-disassembly of the nuclear lamina. *Curr. Opin. Cell Biol.* 4:105–109.

Olins, A. L., D. E. Olins, H. A. Levy, R. C. Durfee, S. M. Margle, E. P. Tinnel, B. E. Hingerty, S. D. Dover, and H. Fuchs. 1984. Modeling Balbiani ring gene transcription with electron microscope tomography. *Eur. J. Cell Biol.* 35:129–142.

Paddy, M. R., A. S. Belmont, H. Saumweber, D. A. Agard, and J. W. Sedat. 1990. Interphase nuclear envelope lamins form a discontinous network that interacts with only a fraction of the chromatin in the nuclear periphery. *Cell.* 62:89–106.

Ramachandran, G. N., and A. V. Lakshminarayanan. 1971. Three-dimensional reconstruction from radiographs and electron micrographs: application of convolutions instead of Fourier transforms. *Proc. Natl. Acad. Sci. USA.* 68:2236–2240.

Skoglund, U., K. Andersson, B. Strandberg, and B. Daneholt. 1986. Three-dimensional structure of a specific pre-messenger RNP particle established by electron microscope tomography. *Nature (Lond.).* 319:560–564.

Snow, C. M., A. Senior, and L. Gerace. 1987. Monoclonal antibodies identify a group of nuclear pore complex glycoproteins. *J. Cell Biol.* 104: 1143–1156.

Sobatka-Briner, C., and D. Chelsky. 1992. COOH-terminal methylation of lamin B and inhibition of methylation by farnesylated peptides corresponding to lamin B and other CAAX motif proteins. *J. Biol. Chem.* 267: 12116–12122.

Woodcock, C. L., B. F. McEwen, and J. Frank. 1991. Ultrastructure of chromatin. II. Three-dimensional reconstruction of isolated fibers. *J. Cell Sci.* 99:107–114.

Yuan, J., G. Simons, G. Blobel, and S. D. Georgatos. 1991. Binding of lamin A to polynucleosomes. *J. Biol. Chem.* 266:9211–9215.